coatings

MDPI

*Article*

# Study on Macro–Meso Shear Characteristics of Geogrid–Silty Clay Interface

**Liang Wang [1], Zhice Zhao [1], Zhaoyun Sun [2], Jincheng Wei [2,*] and Hongxing Li [1]**

[1] Cangzhou Transportation Development (Group) Co., Ltd., Cangzhou 061001, China
[2] Shandong Transportation Research Institute, Jinan 250100, China
* Correspondence: wwjc144632@163.com

**Abstract**

This study investigates the macro–meso shear characteristics of the geogrid–silty clay interface under cyclic loading through a combination of laboratory cyclic direct shear tests and numerical simulations. The effects of geogrid roughness, soil moisture content, shear displacement amplitude, and normal stress on the interface behavior are systematically analyzed. The results show that the interface shear strength and shear stiffness exhibit a three-stage evolution with increasing cycle numbers. This evolution is characterized by rapid attenuation in the early stage, gradual change in the middle stage, and stabilization in the later stage. The main degradation occurs within the first 1–10 cycles, while the interface response tends to stabilize after approximately 25 cycles. Increasing geogrid roughness and normal stress significantly enhances the interface shear strength and restrains cyclic degradation. In contrast, the shear strength reaches a maximum at the optimum moisture content level of 13%. The damping ratio shows an opposite trend to stiffness, increasing with cycle number and gradually approaching stability. Numerical simulation results are in good agreement with the experimental data, with relative errors within 5%. At the mesoscopic level, shear stress is mainly concentrated at the intersections of geogrid ribs, and the soil zone within 0–20 mm above the interface is identified as the primary region of shear deformation.

**Keywords:** geogrid–silty clay interface; cyclic loading; macro–meso shear characteristics; cyclic direct shear test; numerical simulation; shear-strength degradation

## 1. Introduction

Geosynthetic-reinforcement technology has become one of the core methods to improve structural stability and optimize engineering performance in the field of geotechnical engineering. Geogrids, with their unique grid structure and mechanical properties, can effectively restrain soil deformation, transfer stresses, and enhance the overall bearing capacity through friction, mechanical interlocking and bonding effects with the soil. They are widely used in highway subgrades, railway slopes, foundation-pit support, landfill liners and other engineering projects [1–3]. In the geogrid reinforcement system, the interface formed by the geogrid and the soil is a key component for stress transfer and deformation compatibility. Its shear characteristics directly determine the effectiveness of reinforcement and the long-term service safety of the structure [4,5]. Geotechnical structures in practical engineering are often subjected to long-term cyclic loads such as traffic loads, seismic actions, and wave loads. Cyclic loading can induce the degradation of interface shear strength and stiffness, the evolution of cumulative deformation, and variations in energy

Check for updates

Academic Editor: Andrea Nobili

Received: 11 March 2026
Revised: 16 April 2026
Accepted: 23 April 2026
Published: 26 April 2026

**Copyright:** © 2026 by the authors. Licensee MDPI, Basel, Switzerland. This article is an open access article distributed under the terms and conditions of the Creative Commons Attribution (CC BY) license.

dissipation characteristics, which may lead to excessive deformation or even instability and failure of structures [6,7]. Therefore, an in-depth investigation into the shear characteristics of the geogrid–soil interface under cyclic loading is of great practical value in engineering for improving reinforcement design theory and ensuring the long-term stability of engineering projects.

As a widely distributed clay type in East China and South China, silty clay is often used as subgrade filler and slope-soil material due to its abundance and easy access [8]. However, silty clay is characterized by fine particles, strong cohesiveness, and high sensitivity to moisture, with low shear strength and large deformation. It is prone to strength deterioration and cumulative deformation under cyclic loading, which poses a severe challenge to the long-term stability of geogrid-reinforced silty clay structures [9,10]. In contrast to cohesionless soils such as sand and gravel, the interface interaction between silty clay and geogrids involves not only friction and mechanical interlocking, but also the bonding effect induced by inter-particle cohesion, making the interface shear behavior more complicated [11,12]. As a key physical index of silty clay, the variation in moisture content level directly affects the magnitude of inter-particle cohesion and interface-friction characteristics. The repeated action of cyclic loading may lead to the destruction of cohesion, particle rearrangement and cumulative interface damage, thereby significantly changing the interface shear response [13,14].

At present, a certain amount of progress has been made in terms of the research on the shear characteristics of the geogrid–soil interface. However, obvious deficiencies still exist in studies focusing on the interface between geogrids and silty clay, which is a typical cohesive soil. Most existing studies concentrate on the interface characteristics between geogrids and cohesionless soils such as sand and gravel, or improved soils including rubber–sand mixtures and EPS particle–sand mixtures [15,16]. The coupled macro–meso shear mechanism of the silty clay–geogrid interface under cyclic loading has not been fully clarified. On the one hand, the existing studies have not systematically revealed the laws of the macroscopic interfacial shear response under the multi-factor coupling effects of moisture content level, geogrid roughness, normal stress and shear displacement amplitude. In particular, there is a lack of in-depth analysis on interfacial shear stress–displacement hysteretic behavior, volumetric change law, and stiffness and damping evolution under cyclic loading. On the other hand, the research on the meso-mechanisms of interface shear behavior is insufficient, and the internal relationship between the evolution of particle contact force chains, the variation in porosity distribution, energy transfer and dissipation, and the macroscopic shear response during cyclic shearing has not been fully revealed. Furthermore, most existing studies adopt a single experimental method or numerical simulation method, and are lacking macro–meso collaborative analysis combining experiments and simulations. Thus, it is difficult to comprehensively and thoroughly clarify the shear characteristics and interaction mechanism of the geogrid–silty clay interface.

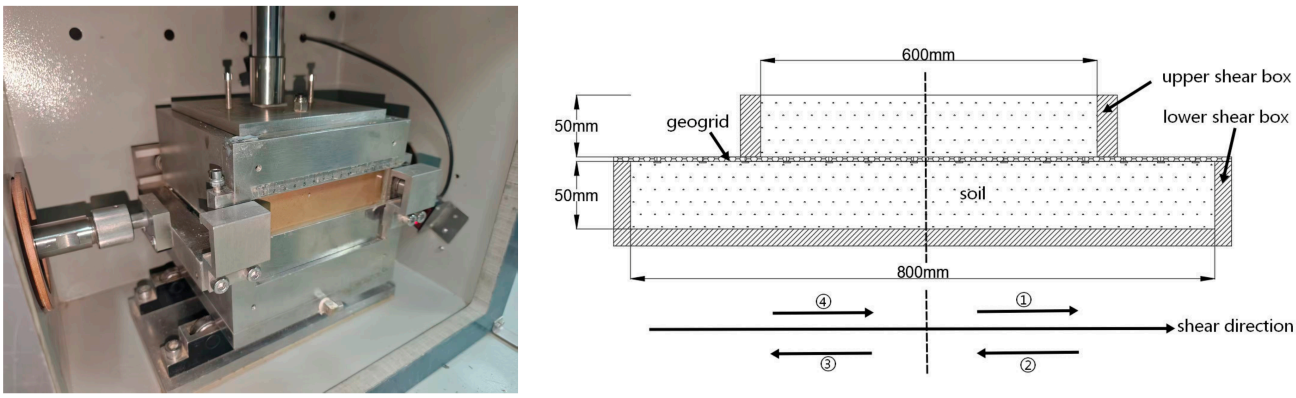
This study focuses on the macro–meso shear characteristics of the geogrid–silty clay interface under cyclic loading. By combining laboratory tests and numerical simulations, the effects of key factors, including geogrid roughness, moisture content level, shear displacement amplitude and normal stress, on the cyclic shear behavior of the interface are systematically investigated. Through laboratory cyclic direct shear tests, the shear stress–shear displacement hysteretic curves and volumetric deformation characteristics of the interface under different test conditions are obtained. The evolution laws of interface shear strength, shear stiffness, damping ratio and energy dissipation characteristics after a number of cycles are analyzed. In this study, the macro scale corresponds to the overall mechanical responses of the interface, such as shear-stress displacement, stiffness and damping, while the meso scale corresponds to the contact-stress distribution between geogrid ribs and soil

particles, the evolution of the soil-plastic-strain field and the development of shear bands. By means of numerical simulation, a meso-scale model of the geogrid–silty clay interface is established, and the relationship between macroscopic shear response and meso-structural evolution is revealed so as to improve the theoretical system of shear characteristics of the geogrid–silty clay interface. This study provides new quantitative insights into the macro–meso cyclic shear mechanism of the geogrid–silty clay interface and clarifies the moisture-dependent dilatancy-contraction transition behavior, which fills the research gap on cohesive soil interfaces under cyclic loading and offers a reliable reference for the design of reinforced-silty-clay subgrades.

## 2. Test Equipment and Program

### *2.1. Test Equipment*

In this study, the TSZ-60 electro-hydraulic servo dynamic direct shear apparatus was used to conduct cyclic direct shear tests on the geogrid–silty clay interface. This equipment is equipped with horizontal–vertical bidirectional closed-loop servo control and supports various loading modes such as constant stress and constant displacement, which can accurately simulate the interface shear behavior under cyclic loading. The equipment mainly consists of a shear box system, a loading system, a measurement system, and a data acquisition system. The three-dimensional model is shown in Figure 1. The dimensions of the upper and lower shear boxes are 600 mm × 200 mm × 50 mm and 800 mm × 200 mm × 50 mm, respectively. The shear displacement amplitude was set to 3 mm, which was determined with reference to related tests [17,18]. The shear frequency was set to 0. 05 Hz. The cyclic shear loading path is ①→②→③→④→① in Figure 1b, where ①→②→③→④ is defined as one full cycle [19].




(**a**) test equipment (**b**) shear box and shear path

**Figure 1.** Direct shear apparatus (Jinan Sanyue, Jinan, China).

### *2.2. Test Materials*

The soil sample was taken from a subgrade engineering site (sampling depth 2–3 m) and is classified as low-liquid-limit silty clay. The sample was stored in a sealed container to prevent moisture loss. Before testing, the soil was air-dried, crushed, and sieved. Distilled water was added according to the designed moisture content level and thoroughly mixed to ensure uniform water distribution. The basic physical properties are listed in Table 1. Polypropylene (PP) biaxial geogrids (Figure 2) were used in the test. The basic properties and designed roughness parameters are shown in Table 2. All soil index properties and geogrid mechanical parameters were tested following standard geotechnical test procedures, using a laser particle size analyzer, direct shear apparatus, electronic universal testing machine and surface roughness tester.

**Table 1.** Basic physical and mechanical properties of silty clay.

| Indicator | Value | Indicator | Value |
|---|---|---|---|
| clay content (<0.005 mm) | 28.60% | optimum moisture content | 13.50% |
| silt content (0.005–0.075 mm) | 62.30% | maximum dry density | 1.87 g/cm$^3$ |
| sand content (>0.075 mm) | 9.10% | liquid limit (wl) | 32.50% |
| plasticity index (PI) | 13.9 | cohesion at natural moisture content c | 28 kPa |
| plastic limit ($w_p$) | 18.60% | internal friction angle at natural moisture content φ | 18.5° |

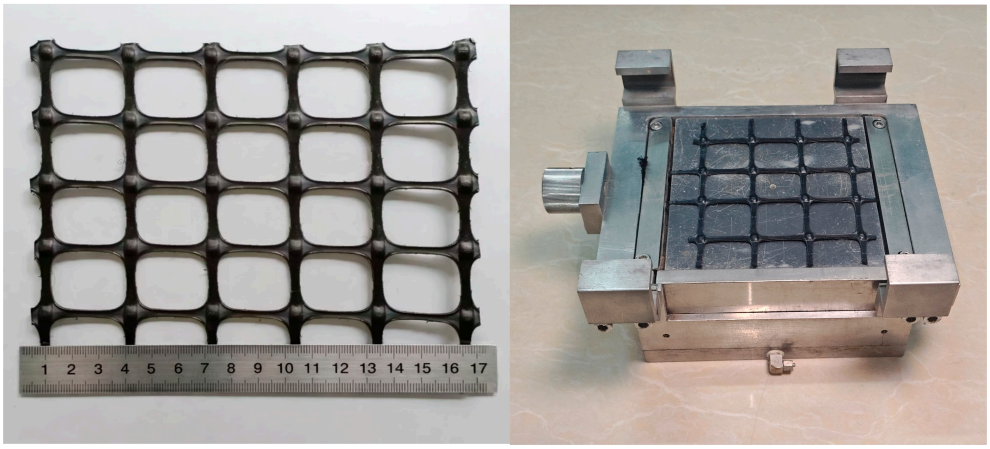



**Figure 2.** Dimensions of the geogrid.

**Table 2.** Basic parameters and roughness design of geogrid.

| Geogrid No. | Treatment Method | Surface Roughness Ra (μm) | Mass per Unit Area (g/m$^2$) | Aperture Size (mm) | Ultimate Tensile Strength (kN/m) | Ultimate Elongation (%) |
|---|---|---|---|---|---|---|
| G1 | unpolished | 0.85 | 280 | 30 × 30 | ≥20 | ≤15 |
| G2 | slightly polished (120 mesh) | 3.26 | 280 | 30 × 30 | ≥20 | ≤15 |
| G3 | heavily polished (80 mesh) | 5.78 | 280 | 30 × 30 | ≥20 | ≤15 |

To investigate the effect of surface roughness on the interfacial shear characteristics, three types of geogrid specimens with gradient roughness were prepared by sandpaper polishing. The arithmetic mean deviation (Ra) of the surface was measured using a roughness tester to obtain significantly different roughness variables [20]. Before testing, the geogrid was cut into rectangular specimens of 800 mm × 200 mm to match the size of the lower shear box. It was then fixed at the bottom of the lower shear box, with the edges secured using steel pressure plates and bolts to prevent sliding or wrinkling during shearing, ensuring effective contact at the geogrid–soil interface.

### *2.3. Test Program*

In this test, static loading was applied in the normal direction and sinusoidal cyclic loading in the shear direction to simulate the coupling of static normal stress and cyclic shear load on the geogrid–silty clay interface in practical engineering. The loading frequency was fixed at 0.5 Hz to simulate traffic loads, with 60 cyclic shear cycles. Data at the 1st, 5th, 10th, 25th, and 50th cycles were collected for subsequent analysis of the evolution of interfacial shear characteristics [21]. In this test, roughness, soil moisture content, shear displacement amplitude, and normal stress were taken as the key variables, with three levels set for each variable. The loading frequency and number of cycles were fixed. The detailed test design is shown in Table 3.

**Table 3.** Variables and levels design of orthogonal test.

| Variable Type | Level 1 | Level 2 | Level 3 |
|---|---|---|---|
| geogrid roughness/G | G1 (Ra = 0.85 μm) | G2 (Ra = 3.26 μm) | G3 (Ra = 5.78 μm) |
| moisture content of silty clay/w (%) | 10% | 13% | 16% |
| normal stress/f (kPa) | 50 | 100 | 150 |
| fixed parameters | loading frequency: 0.5 Hz, number of cycles: 60 (data from the 1st, 5th, 10th, 25th, and 50th cycles are analyzed). | | |

This test was conducted in accordance with the design principles specified in ISO/TR 18228-5:2025, BS 8006 and BRE BR470. The obtained macro–meso shear laws of the geogrid–silty clay interface can be combined with the soil–geosynthetic interaction framework in these standards. The results provide quantitative reference for the design of reinforced structures, and can be applied to the stability evaluation of embankments and slopes under cyclic loading in engineering practice.

The detailed test procedure consists of the following six steps:

(1) Specimen forming and geogrid fixation: The prepared silty clay was compacted layer by layer into the upper shear box, with strict control of dry density and filling thickness. The geogrid was fixed flatly at the bottom of the lower shear box, and the upper and lower shear boxes were assembled to ensure effective contact at the geogrid–soil interface.

(2) Equipment debugging and precision calibration: The assembled shear box was mounted on the test bench, and the loading, measurement and data acquisition systems were connected. The servo control function of the equipment was debugged, and the measurement accuracy of stress and displacement was calibrated to ensure no abnormal operation.

(3) Normal preloading and stress equilibrium: The designed static normal load was applied and maintained until the normal displacement of the soil sample stabilized, eliminating initial pore deformation and allowing the specimen to reach a stress equilibrium state.

(4) Cyclic shear and loading: The normal stress was kept constant, and the horizontal loading system was activated. Sinusoidal cyclic shear load was applied at the designed shear displacement amplitude to complete 60 cycles of continuous shear loading. Full monitoring and data acquisition: The data acquisition system was operated throughout the test to synchronously record key indicators such as shear stress and shear displacement, with emphasis on capturing complete data curves at the specified number of cycles.

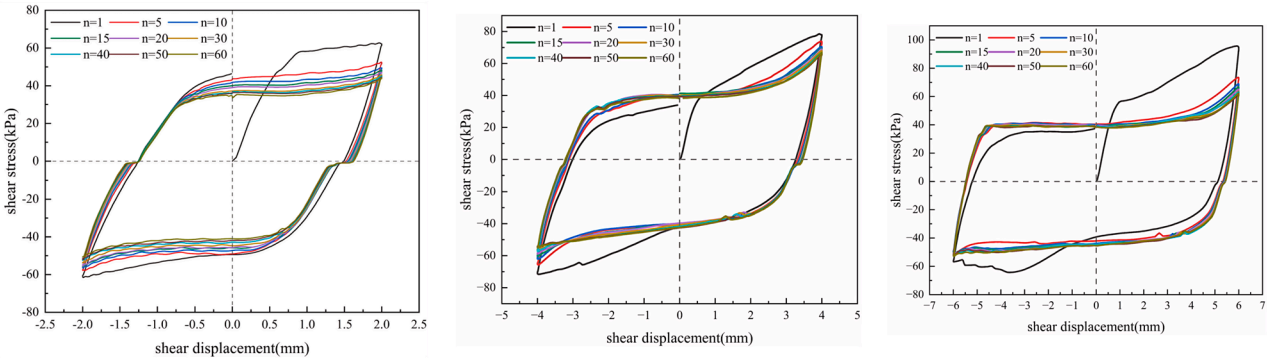
(5) Load unloading and equipment reset: Upon completion of cyclic shear, the normal and horizontal loads were gradually removed. The shear box was disassembled and cleaned, and the test equipment was cleaned and reset. Preliminary sorting of test data was then conducted.

To reduce accidental errors in the test, the test results were taken as the average of three parallel tests. If the deviation exceeded 5%, the test was repeated. Through the above test procedure, cyclic direct shear tests were completed for all orthogonal groups. Complete cyclic shear data for the geogrid–silty clay interface under different variable combinations were obtained, which lays a data foundation for the subsequent analysis of macroscopic shear characteristics and the investigation of meso-mechanisms of the interface.

## 3. Macroscopic Shear Characteristics

### *3.1. Relationship Between Shear Stress and Shear Displacement*

As shown in Figure 3, under the same conditions, the interface peak shear stress increases and the hysteresis loop becomes fuller with increasing geogrid roughness. The peak shear stress of G3 geogrid is approximately 42. 6% higher than that of G1. The attenuation amplitude is the largest during the 1st to 10th cycles, and the attenuation rate decreases with increasing roughness. High-roughness geogrids can effectively inhibit the degradation of interface shear strength. This indicates that increasing roughness significantly enhances the mechanical interlocking between the geogrid and silty clay. The protrusions on the rough surface form a tighter interlock with soil particles, requiring greater resistance to be overcome during shearing, while the interparticle friction is also improved.

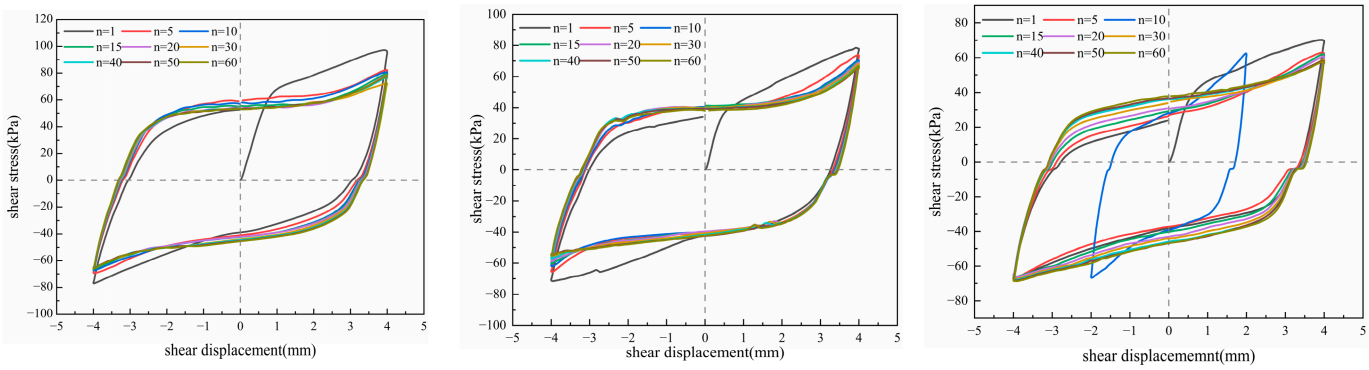



(**a**) G1 (**b**) G2 (**c**) G3

**Figure 3.** Hysteretic curves for various cycle numbers under different roughness conditions.

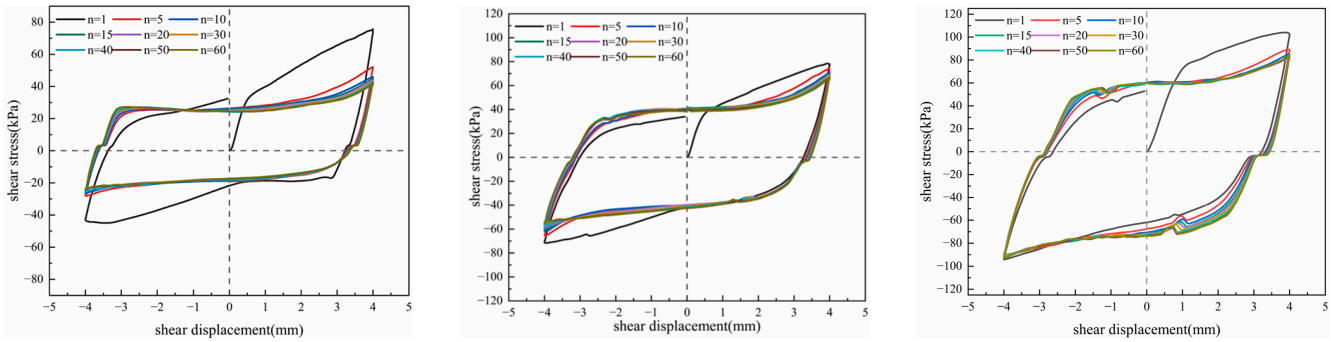
As shown in Figure 4, under identical test conditions, the interfacial peak shear stress reaches its maximum value at a moisture content level of 13%. With an increase in moisture content, the water film between soil particles becomes thicker, resulting in a significant reduction in cohesion. The lubrication effect of pore water facilitates the slippage of soil particles. Meanwhile, the interfacial contact pressure between the geogrid and soil is partially counteracted by pore water, which greatly weakens the mechanical interlocking and friction, thus leading to an obvious decrease in the interfacial peak shear stress. Under the same conditions, the interfacial peak shear stress first increases rapidly and then gradually stabilizes with the increase in shear displacement amplitude. The hysteresis loop evolves from narrow and slender to full and plump, with a significant increase in its area. When the displacement amplitude increases to 3 mm, the relative interfacial slip is enhanced, the cohesion between soil particles is gradually lost, and the mechanical interlocking between the geogrid and soil is fully mobilized, resulting in a rapid improvement of the interfacial shear strength. At 5 mm, the peak shear stress tends to be stable, at which point the interfacial shear strength is mainly dominated by the combined action of dynamic friction and mechanical interlocking.

As shown in Figure 5, under the same conditions, the interfacial peak shear stress increases with increasing normal stress. The difference between the upper and lower limits of the hysteresis loop and the area of the hysteresis loop both increase accordingly. The peak shear stress at 150 kPa is approximately 31.2% higher than that at 100 kPa and 78.5% higher than that at 50 kPa. The compression effect of normal stress makes soil particles embed more tightly into the rough surface and grid structure of the geogrid, significantly enhancing the mechanical interlocking. Meanwhile, the contact pressure between soil particles increases, and the cohesion between particles is more fully mobilized. These factors jointly promote the improvement of interfacial shear strength.




(**a**) w = 10% (**b**) w = 13% (**c**) w = 16%

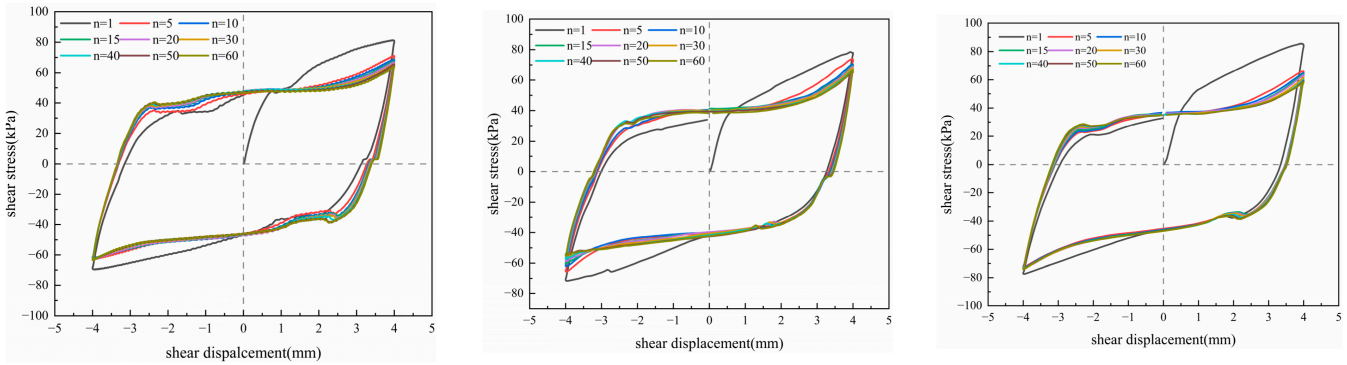
**Figure 4.** Hysteretic curves for various cycle numbers under different moisture contents.




(**a**) f = 50 kPa (**b**) f = 100 kPa (**c**) f = 150 kPa

**Figure 5.** Hysteretic curves for various cycle numbers under different normal stresses.

The effect of loading frequency on the interfacial peak shear stress is relatively minor. As the soil possesses certain viscoelastic properties, a lower loading frequency corresponds to a longer duration of cyclic shear, which provides sufficient time for soil particle sliding, rearrangement, and pore water migration, leading to more significant energy dissipation during the shearing process. Therefore, loading frequency is not a critical factor governing the cyclic evolution of interfacial shear strength (Figure 6).



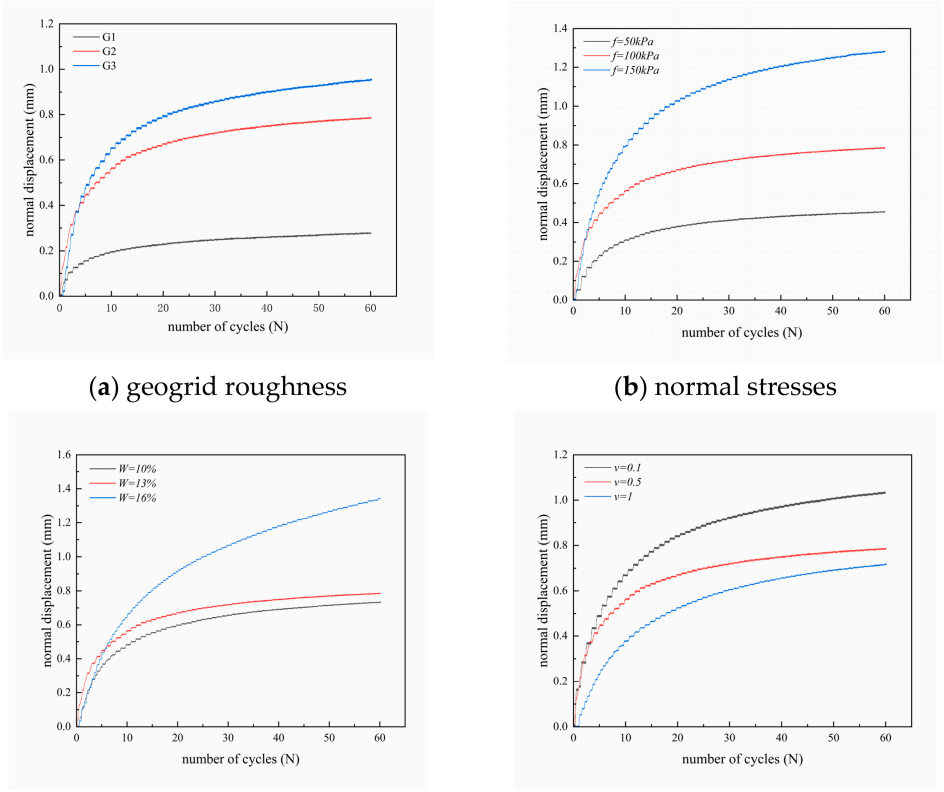

(**a**) v = 0.1 (**b**) v = 0.5 (**c**) v = 1

**Figure 6.** Cyclic shear hysteretic curves under different loading rates.

### *3.2. Evolution Law of Interface-Volume Deformation Under Cyclic Loading*

The volume change behavior of the geogrid–silty clay interface is characterized by the normal (vertical) displacement of the soil sample during cyclic shear, where a positive normal displacement indicates dilatancy, while a negative value represents contraction.

This macroscopic volume response essentially reflects the coupled evolution of soil particle arrangement, porosity variation, and the mechanical interlocking state between the geogrid and soil particles under cyclic shear. To systematically quantify the cyclic evolution law of interface-volume deformation under the coupling of multiple influencing factors, the curves of the maximum normal displacement of the interface with the number of cycles under different working conditions are plotted in Figure 7, which covers four key variables: geogrid roughness, soil moisture content, normal stress, and loading frequency.




(**a**) geogrid roughness (**b**) normal stresses

(**c**) water content (**d**) loading rates

**Figure 7.** Relationship curve between normal displacement and cycle number under different working conditions.

As shown in Figure 7, the maximum normal displacement of the interface under all test conditions presents a consistent three-stage evolution law with the increase in cycle numbers. The first stage is the rapid growth stage (1st to 10th cycles): the normal displacement increment in this stage accounts for more than 70% of the total cumulative increment, which is attributed to the rapid failure of the initial bonding between soil particles, the sharp increase in particle sliding and rearrangement, and the continuous mobilization of the uplifting effect of geogrid ribs on the surrounding soil. The second stage is the slow growth stage (10th to 25th cycles): with the gradual stabilization of soil particle arrangement, the growth rate of normal displacement decreases significantly, and the interface dilatancy effect develops slowly. The third stage is the stable convergence stage (after the 25th cycle): the fluctuation of the maximum normal displacement is less than 5% with the further increase in cycle numbers, the soil particle arrangement reaches a dynamic equilibrium state, the porosity no longer changes significantly, and the interface-volume-change effect tends to be stable. This three-stage evolution law is highly consistent with the cyclic degradation characteristics of interface shear strength and shear stiffness, revealing the intrinsic correlation between interface-volume deformation and shear mechanical response.

Geogrid roughness imposes a significant enhancement effect on the interface dilatancy, as shown in Figure 7a. Under the same number of cycles, the maximum normal

displacement and the dilatancy effect increase significantly with the rise of geogrid surface roughness. After 50 cycles, the maximum normal displacement of the G3 geogrid (Ra = 5.78 μm) reaches 2.8 mm, which is much higher than that of G2 (Ra = 3.26 μm) and G1 (Ra = 0.85 μm) geogrids. The high-roughness surface of the geogrid forms a tighter mechanical interlock with soil particles, and the squeezing and uplifting effect on the soil during cyclic shear is more significant, leading to a more obvious increase in soil porosity and a more prominent dilatancy effect. Meanwhile, the higher the geogrid roughness, the faster the dilatancy effect reaches stability, which is because the high-roughness interface can fully mobilize the interlocking effect with soil particles in fewer cycles.

Normal stress shows a strong inhibitory effect on the interface dilatancy, as presented in Figure 7b. The greater the normal stress, the smaller the maximum normal displacement of the interface and the weaker the dilatancy effect. After 50 cycles, the maximum normal displacement under 150 kPa normal stress is only 0.9 mm, which is 57.1% lower than that under 50 kPa normal stress. The compression effect induced by high normal stress makes the soil particles arrange more densely, and the uplifting effect of the geogrid rough surface on the soil can hardly overcome the constraint of normal stress, making it difficult for the soil porosity to increase; thus, significantly suppressing the dilatancy effect. In addition, the increment of normal displacement with the number of cycles decreases with the increase in normal stress, and the interface volume change can reach a stable state in fewer cycles under high normal stress.

Moisture content level is the core controlling factor of the interface-volume-change characteristics, and its influence law is shown in Figure 7c. When the moisture content level is 10%, the interface shows significant dilatancy, with a maximum normal displacement of 2.2 mm; at the optimum moisture content level of 13%, the interface presents slight dilatancy, with a maximum normal displacement of 1.5 mm; and when the moisture content level rises to 16%, the interface exhibits mild contraction, with a maximum normal displacement of −0.4 mm. The intrinsic mechanism of this difference lies in the variation in soil physical properties with moisture content level: at low moisture content levels, the soil has high cohesion and low plasticity, and soil particles are prone to be lifted along the rough surface of the geogrid during shear, resulting in significant dilatancy; at high moisture content levels, the soil has low cohesion and high plasticity, the sliding of soil particles fills the internal pores of the soil, and the lubrication effect of pore water weakens the uplifting effect of the geogrid, eventually leading to volume contraction; at the optimum moisture content level, the bonding effect and sliding tendency of soil particles reach an equilibrium state; thus, the dilatancy effect is the weakest.

The influence of loading frequency on the interface volume change is relatively minor within the test range, as shown in Figure 7d. A higher loading frequency corresponds to a slightly smaller normal displacement and a weaker dilatancy effect, and the maximum normal displacement at 0.5 Hz is approximately 12.3% lower than that at 0.1 Hz after 50 cycles. This is because the soil has certain viscoelastic properties: at low frequencies, the duration of a single shear cycle is longer, which provides sufficient time for soil particle sliding, rearrangement and porosity evolution, allowing the dilatancy effect to be fully mobilized; and at high frequencies, the short duration of shear action prevents soil particles from being fully lifted, resulting in a limited increase in porosity. It should be noted that the cyclic evolution trend of interface volume change remains consistent under different loading frequencies, indicating that loading frequency is not a key factor controlling the cyclic evolution of interface-volume deformation.

A significant positive correlation exists between the interface-volume-change behavior and the shear strength: the more pronounced the dilatancy effect, the higher the interface peak shear strength. The dilatancy effect loosens the arrangement of soil particles near the

interface, strengthens the mechanical interlocking between the geogrid and the soil, and increases the interface dynamic friction coefficient, thereby enhancing the interface shear strength. Conversely, volume contraction weakens the mechanical interlocking between the geogrid and soil particles, resulting in a reduction in interface shear strength. Thus, the volume change characteristics can be used as an important macroscopic indicator to reflect the mobilization degree of interface friction and mechanical interlocking effects under cyclic loading.

### *3.3. Interfacial Shear Stiffness and Damping Ratio*

#### 3.3.1. Interfacial Shear Stiffness

The secant stiffness method is adopted to calculate the shear stiffness. This method can effectively reflect the average deformation resistance of the interface at the elastoplastic stage under cyclic loading, and avoid the drastic fluctuation of tangent stiffness in the plastic stage, making it a common approach for evaluating the shear stiffness of geogrid–soil interfaces. Based on the shear stress–shear displacement hysteresis loops corresponding to various cycle numbers (1, 5, 10, 25, and 50 cycles). The secant slope at 50% of the shear displacement amplitude in each hysteresis loop is selected as the interfacial shear stiffness for that cycle. The formula is given as follows:

$$K = \frac{\tau}{\delta} \quad (1)$$

In the formula, $K$ is the interfacial shear stiffness, kPa/mm, $\tau$ is the shear stress at 50% of the displacement amplitude, kPa, $\delta$ is 50% of the shear displacement amplitude, mm. The calculated results are presented in Table 4.

**Table 4.** Calculated results for shear stiffness for the geogrid–silty clay interface (kPa/mm).

| Test Variable Combinations | Number of Cycles | | | | |
|---|---|---|---|---|---|
| | 1 Cycles | 5 Cycles | 10 Cycles | 25 Cycles | 50 Cycles |
| G1-10-1 | 38.26 | 32.58 | 29.65 | 28.92 | 28.75 |
| G1-13-1 | 42.35 | 37.86 | 35.12 | 34.25 | 34.08 |
| G1-16-1 | 26.58 | 22.35 | 20.18 | 19.52 | 19.36 |
| G2-10-3 | 25.68 | 22.15 | 20.36 | 19.82 | 19.65 |
| G2-13-3 | 29.85 | 26.52 | 24.86 | 24.18 | 24.02 |
| G2-16-3 | 18.36 | 15.25 | 13.82 | 13.26 | 13.15 |
| G3-10-5 | 15.28 | 13.36 | 12.52 | 12.18 | 12.05 |
| G3-13-5 | 18.65 | 16.82 | 15.96 | 15.62 | 15.5 |
| G3-16-5 | 10.35 | 8.92 | 8.26 | 7.98 | 7.86 |
| G2-13-3-50 | 20.58 | 17.86 | 16.52 | 16.05 | 15.92 |
| G2-13-3-100 | 29.85 | 26.52 | 24.86 | 24.18 | 24.02 |
| G2-13-3-150 | 38.62 | 35.25 | 33.86 | 33.22 | 33.05 |

The interfacial shear stiffness exhibits a distinct evolutionary pattern characterized by rapid attenuation in the early stage, slow attenuation in the middle stage, and gradual stabilization in the later stage with increasing number of cycles. The stiffness degradation mainly occurs within the 1st to 10th cycles, during which the attenuation accounts for more than 75% of the total attenuation. After 25 cycles, the variation in stiffness is less than 1%, indicating that no obvious degradation occurs. This evolution law originates from the rapid failure of interfacial bonding, the sliding and rearrangement of soil particles, and the loss of local interlocking at the initial stage of cyclic shear. In the later stage, the particle arrangement and geogrid–soil interlocking reach a dynamic equilibrium, and the cumulative interface damage approaches a limit state. Various factors impose significant influences on the interfacial stiffness: greater geogrid roughness induces stronger interfacial

interlocking, resulting in higher shear stiffness and a slower attenuation rate. At the optimum moisture content level of 13%, the cohesion and particle arrangement are optimal, leading to much higher stiffness than those at 10% (low moisture content) and 16% (high moisture content). A smaller shear displacement amplitude corresponds to a dominance of elastic deformation at the interface and, thus, a higher stiffness. The normal stress shows an approximately linear positive correlation with shear stiffness. High normal stress enhances the interfacial contact compactness, restrains particle sliding, and, thus, significantly improves the stiffness and reduces the attenuation rate.

#### 3.3.2. Damping Ratio

The damping ratio is determined by the ratio of the energy dissipation in a single cycle to the elastic strain energy of the equivalent elastic body, and is calculated using the energy method (Rayleigh damping method). The formula is given as follows:

$$D = \frac{1}{4\pi} \cdot \frac{Wd}{We} \tag{2}$$

$$Wd = \frac{1}{2}\left|\sum_{i=1}^{n}(\delta i + 1 - \delta i)(\tau i + 1 + \tau i)\right| \times 10^{-3} \tag{3}$$

$$We = \frac{1}{2}\tau max \cdot \delta max \tag{4}$$

In the formula, D is the damping ratio. Wd is the energy dissipation, $J/m^2$. We is the elastic strain energy, $J/m^2$.

For each test group with different variable combinations, the damping ratio at the 1st, 5th, 10th, 25th, and 50th cycles was calculated sequentially. The calculated results are presented in Table 5. The interfacial damping ratio shows a significant inverse trend with the evolution of shear stiffness, and exhibits a three-stage variation pattern with increasing number of cycles: rapid increase, slow growth, and stable convergence. The 1st to 10th cycles constitute the main increasing stage of the damping ratio, during which the increment accounts for more than 70% of the total increment. After 25 cycles, the variation is less than 0. 005, indicating that the damping ratio has entered a stable range. At the initial stage of cycling, the interfacial bonding is degraded, soil particles slide and rearrange, and the interlocking between geogrid and silty clay is gradually mobilized. As a result, the energy dissipation paths continuously expand, and the energy absorption capacity is improved. In the later stage, the bonding is completely destroyed, the particle arrangement and interlocking reach a dynamic equilibrium, and the energy dissipation state tends to be stable. The damping ratio increases with the rise of geogrid roughness, soil moisture content level and shear displacement amplitude. Conversely, the increase in normal stress restricts particle sliding and leads to a dominance of static friction at the interface, thereby reducing energy dissipation and significantly lowering the damping ratio.

### *3.4. Interfacial Energy Dissipation*

To characterize the ability of the interface to absorb and dissipate external energy during cyclic shear, the single-cycle energy dissipation and cumulative energy dissipation are adopted as evaluation indices. The energy dissipation characteristics are quantified based on the shear stress–shear displacement hysteretic loops, and their evolution with the number of cycles, as well as the influence mechanism of each test variable, are analyzed. Under cyclic shear, the interfacial energy dissipation mainly arises from the degradation and reestablishment of interparticle bonding, frictional sliding between the geogrid and soil as well as among soil particles, and particle rearrangement and structural deformation induced by mechanical interlocking. The total cumulative interfacial energy dissipation

(Wtotal) is the sum of the energy dissipation in each single cycle, and its calculation formula is given as follows:

$$Wtotal = \sum_{k=1}^{m} Wd(k) \quad (5)$$

In the formula, m is number of cycles. $W_d$ (k) is energy dissipation in the k-th cycle, $J/m^2$.

**Table 5.** Calculated results of damping ratio for the geogrid–silty clay interface.

| Test Variable Combination (Roughness–Moisture Content–Displacement Amplitude) | Number of Cycles | | | | |
|---|---|---|---|---|---|
| | 1 Cycles | 5 Cycles | 10 Cycles | 25 Cycles | 50 Cycles |
| G1-10%-1 mm | 0.125 | 0.158 | 0.172 | 0.178 | 0.18 |
| G1-13%-1 mm | 0.118 | 0.145 | 0.156 | 0.16 | 0.162 |
| G1-16%-1 mm | 0.186 | 0.225 | 0.242 | 0.248 | 0.25 |
| G2-10%-3 mm | 0.165 | 0.202 | 0.218 | 0.225 | 0.228 |
| G2-13%-3 mm | 0.152 | 0.186 | 0.2 | 0.205 | 0.208 |
| G2-16%-3 mm | 0.228 | 0.265 | 0.282 | 0.288 | 0.29 |
| G3-10%-5 mm | 0.205 | 0.242 | 0.26 | 0.268 | 0.27 |
| G3-13%-5 mm | 0.192 | 0.228 | 0.245 | 0.252 | 0.255 |
| G3-16%-5 mm | 0.265 | 0.302 | 0.32 | 0.328 | 0.33 |
| G2-13-3-50 | 0.186 | 0.225 | 0.242 | 0.248 | 0.25 |
| G2-13-3-100 | 0.152 | 0.186 | 0.2 | 0.205 | 0.208 |
| G2-13-3-150 | 0.125 | 0.158 | 0.172 | 0.178 | 0.18 |

As shown in Figure 8, under different test variable combinations, the single-cycle energy dissipation at the geogrid–silty clay interface presents a consistent evolutionary trend with the number of cycles. The interfacial energy dissipation increases rapidly within 0–10 cycles and tends to be stable after 25 cycles. This evolution is consistent with the mechanism involving the failure of initial interfacial bonding, the sliding and rearrangement of soil particles, and the achievement of dynamic equilibrium in mechanical interlocking. Each test variable exerts a significant regulatory effect on interfacial energy dissipation. Increases in geogrid roughness, silty clay moisture content, shear displacement amplitude, and normal stress all lead to corresponding rises in interfacial energy dissipation and its stable value, among which the influence of shear displacement amplitude is the most prominent. In contrast, the loading frequency has no significant effect on the interfacial energy dissipation characteristics.

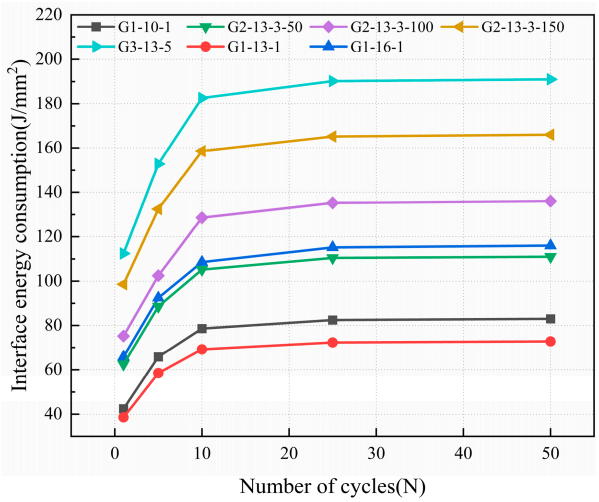



**Figure 8.** Evolution characteristics of single-cycle energy dissipation at the geogrid–silty clay interface with number of cycles.

## 4. Mesoscopic Characteristics

### *4.1. Model Introduction and Calibration*

#### 4.1.1. Numerical Model Construction

This numerical simulation is implemented using the transient structural module in ANSYS Workbench 2024 R2 for transient dynamic cyclic shear analysis. Based on the geometric dimensions and test conditions of the laboratory cyclic direct shear test, a mesoscopic model for the cyclic shear of the geogrid–silty clay interface was established. The overall dimensions of the model are 800 mm × 200 mm × 100 mm (length × width × height), which is consistent with the size of the laboratory shear box. The model is divided into three parts: the upper soil zone, the geogrid zone, and the base zone of the lower shear box, as illustrated in Figure 9.

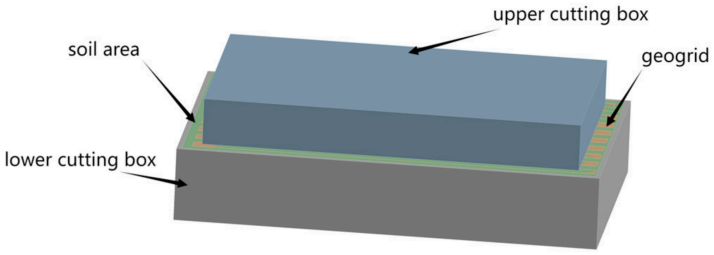



**Figure 9.** Cyclic shear model of the geogrid–silty clay interface.

The soil was treated as a continuous elastoplastic medium; the geogrid was linear elastic without damage; and interface contact obeyed Coulomb friction. Boundary conditions: the lower box was fully fixed, the upper box was constrained vertically and laterally with free horizontal shear, and constant normal stress was applied on the soil top.

The silty-clay specimen adopts the Modified Cam-Clay (MCC) model as its constitutive model. This model can accurately describe the elastoplastic deformation, shear yielding, dilation, and contraction characteristics of cohesive soil under cyclic loading, which is highly compatible with the mechanical behavior of the low-liquid-limit silty clay used in the tests. The geogrid is simulated using a linear elastic constitutive model. No obvious plastic deformation occurred in the geogrid during the tests, and the linear elastic model can effectively represent its mechanical deformation behavior. The upper and lower shear boxes are regarded as rigid bodies, with corresponding displacement boundaries and constraint conditions applied. The interface contact between the geogrid and silty clay is implemented using the surface-to-surface contact algorithm. The normal behavior is defined as hard contact, which allows separation of the contact surfaces under tension and prevents penetration under compression. The tangential behavior follows the Coulomb friction model, and different geogrid roughness levels are simulated by adjusting the interfacial friction coefficient. The interfacial friction coefficients corresponding to the three geogrids G1, G2, and G3 are set to 0.32, 0.40, and 0.48, respectively, showing a positive correlation with the roughness gradient. A bonded constraint is applied between the silty clay specimen and the inner wall of the upper shear box to eliminate relative sliding between the specimen and the shear box during testing. The geogrid is fully fixed to the top surface of the lower shear box to simulate the fixing effect of bolts and steel plates in the laboratory tests, thereby avoiding sliding or wrinkling of the geogrid during shear.

The loading protocol exactly reproduces the loading path of the laboratory tests, and cyclic shear loading is applied using the transient dynamic analysis module. The entire loading process is divided into two stages. The first stage is the normal preloading stage. A constant uniform normal stress is applied on the top surface of the upper shear box, with three levels set at 50 kPa, 100 kPa, and 150 kPa, respectively. Normal stress is maintained

until the vertical displacement of the soil tends to be stable, eliminating the initial pore deformation of the specimen and achieving a stress equilibrium state consistent with the laboratory tests. The second stage is the cyclic shear stage. With the normal stress kept constant, a horizontal cyclic displacement load in the form of a sine wave is applied to the lower shear box. The displacement amplitudes are set at three levels (1 mm, 3 mm, and 5 mm), the loading frequency is fixed at 0.5 Hz, and the total number of cycles is set to 60, which is fully consistent with the laboratory test loading scheme. During the calculation, the results of the 1st, 5th, 10th, 25th, and 50th cycles are mainly extracted for comparative analysis and mechanism verification with the laboratory test data.

The silty clay is described by the Modified Cam-Clay (MCC) model, which can accurately characterize the elastoplastic deformation, shear yielding, dilatancy and contraction characteristics of cohesive soil under cyclic loading, and is highly compatible with the mechanical behavior of low-liquid-limit silty clay in this study. Based on the critical state soil mechanics theory, the model takes plastic volumetric strain and plastic shear strain as hardening parameters, and defines the yield and failure criteria of soil through the normal consolidation line and critical state line. The geogrid was assumed to be a linear elastic material with no obvious plastic deformation during the test. The upper and lower shear boxes were set as rigid bodies, and the surface-to-surface contact algorithm was adopted for the geogrid–soil interface with hard contact in the normal direction and the Coulomb friction model in the tangential direction.

#### 4.1.2. Model Parameter Calibration

The core parameters of the numerical model are classified into three categories: the constitutive parameters of silty clay, the material parameters of the geogrid, and the geogrid–soil interface contact parameters. All parameters are calibrated against laboratory test results to ensure that the physical and mechanical properties of the numerical model are fully consistent with those of the test materials. The core parameters of the Modified Cam-Clay model for silty clay are calibrated based on laboratory geotechnical tests. The slope of the critical state line is calculated from the internal friction angle of 18.5° at a natural moisture content level. The compression index and rebound index are determined by fitting the results of consolidation tests. The initial void ratio is derived from the maximum dry density of 1.87 g/cm$^3$ of the test soil sample. The effective cohesion and effective internal friction angle are directly adopted from the measured data of laboratory direct shear tests. The detailed calibrated parameters are listed in Table 6. The material parameters of the geogrid are determined from the property tests of a polypropylene geogrid. The elastic modulus is set to 1.2 GPa and the Poisson's ratio is 0.33, matching the mechanical properties of the geogrid used in the tests. The specific parameters are presented in Table 7. Specifically, all material property values listed in the following Tables 6 and 7 and Figure 10 are directly derived from the laboratory tests conducted in this study.

**Table 6.** Calibration results of Modified Cam-Clay-model parameters for silty clay.

| Parameter Name | Symbol | Value | Parameter Source |
|---|---|---|---|
| Slope of critical state line | M | 0.92 | calculated from the internal friction angle $\varphi$ = 18.5° at natural moisture content. |
| Compression index | $\lambda$ | 0.078 | fitted from laboratory consolidation test results. |
| Rebound index | $\kappa$ | 0.012 | fitted from laboratory consolidation test results. |
| Initial void ratio | $e_0$ | 0.38 | calculated from the maximum dry density of 1.87 g/cm$^3$ |
| Poisson's ratio | $\nu$ | 0.35 | empirical values of silty clay combined with test calibration. |
| Effective cohesion | c′ | 28 kPa | measured by laboratory direct shear test. |
| Effective internal friction angle | $\varphi'$ | 18.5° | measured by laboratory direct shear test. |

**Table 7.** Calibration results for material and interface contact parameters for geogrid.

| Parameter Name | Value | Parameter Source |
|---|---|---|
| Elastic modulus | 1.2 GPa | test results of polypropylene geogrid |
| Poisson's ratio | 0.33 | polypropylene material |
| Geogrid thickness | 5 mm | measured values of the geogrid used in tests |
| Interface-friction coefficient between G1 geogrid and soil | 0.32 | test results |
| Interface-friction coefficient between G2 geogrid and soil | 0.4 | test results |
| Interface-friction coefficient between G3 geogrid and soil | 0.48 | test results |

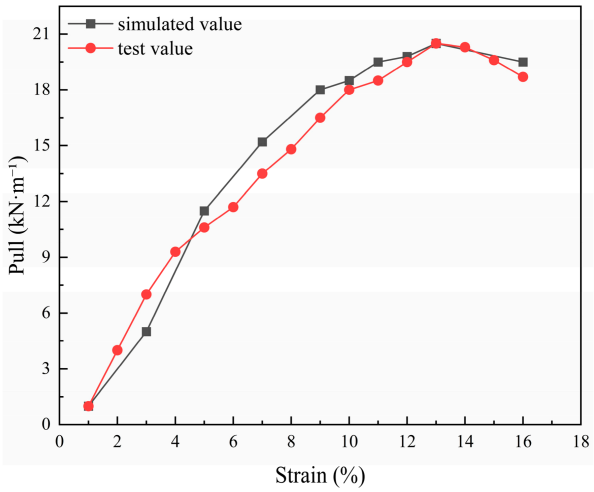
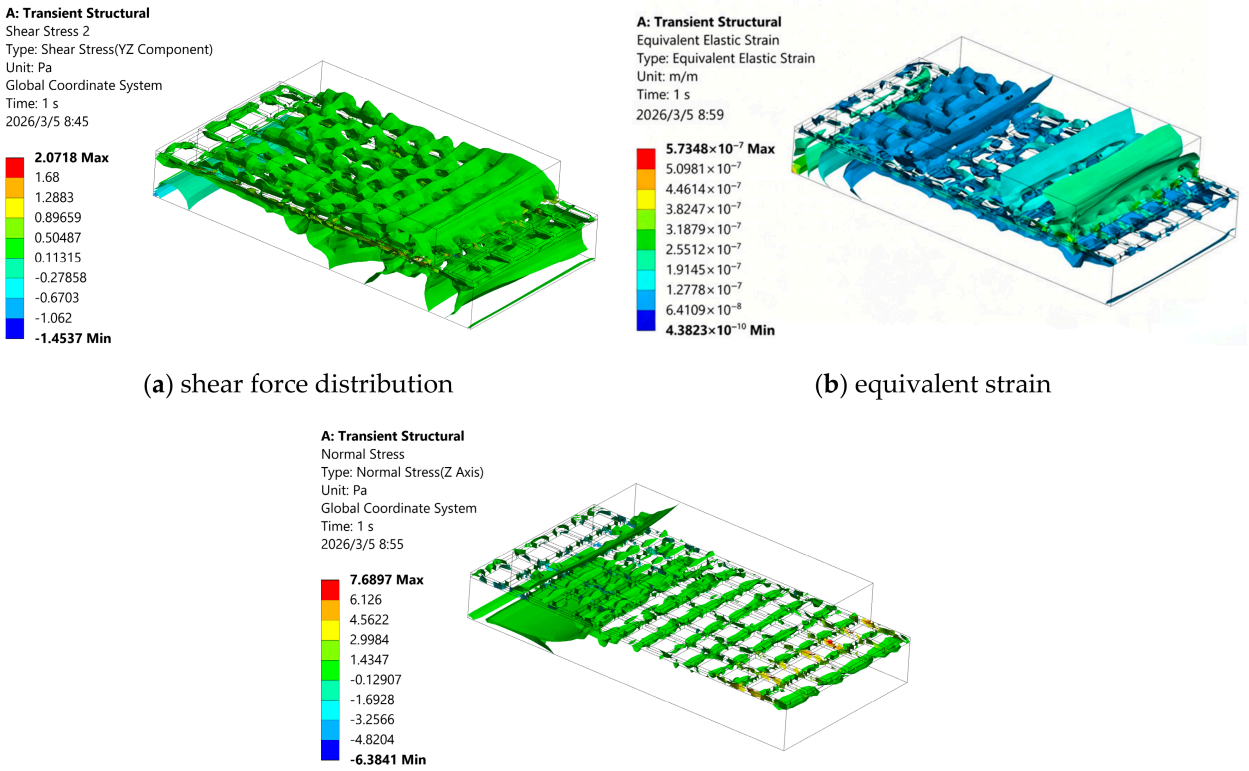



**Figure 10.** Comparison of simulated and experimental tensile force and strain of geogrid.

*4.2. Analysis of Interfacial Contact-Stress Distribution and Shear-Strength Characteristics*

Based on the calibrated numerical model, the contact-stress-distribution nephograms and shear-stress-evolution data at the geogrid–soil interface during the entire cyclic shear process were extracted using the contact tool, as shown in Figure 11. During cyclic shear, the shear stress at the geogrid–soil interface exhibits an obvious non-uniform distribution. Shear stress is mainly concentrated at the intersections of the geogrid transverse ribs and longitudinal ribs, where the mechanical interlocking effect is the most significant. The peak shear stress in these regions is more than 40% higher than that in the middle parts of the geogrid ribs. In contrast, the shear stress at the contact interface between the soil inside the geogrid apertures and the geogrid remains at a low level. This indicates that the shear resistance of the soil provided by the geogrid is mainly due to the friction and mechanical interlocking between the geogrid ribs and the soil, demonstrating the enhancement effect of the geogrid aperture structure on the interfacial shear strength. From the perspective of cyclic evolution, at the peak shear moment of the 1st cycle, the interfacial shear stress distribution is highly non-uniform with significant local stress concentration, and the maximum shear stress reaches 82 kPa. With an increasing number of cycles, at the 10th cycle, the stress concentration is obviously alleviated due to the rearrangement of soil particles and the gradual failure of the initial interfacial bonding. The shear stress distribution on the interface tends to be uniform, and the peak shear stress decreases to 71 kPa. The interfacial stress distribution characteristics differ significantly among geogrids with different roughness levels. The interface shear stress distribution of the G3 high-roughness geogrid is more uniform. The effective contact area between the geogrid and soil is increased by 35% compared with the unpolished G1 geogrid. The stress concentration

coefficient is significantly reduced, and the overall average interfacial shear stress is much higher than that of low-roughness geogrids.




(**a**) shear force distribution (**b**) equivalent strain

(**c**) normal stress distribution

**Figure 11.** Contours of stress and strain distribution.

Through numerical simulation, the interfacial peak shear stress under different working conditions of moisture content level, normal stress and shear displacement amplitude was systematically calculated and quantitatively compared with laboratory test results, as shown in Table 8. The relative errors between the simulated and experimental values under different working conditions are all controlled within 5%. The interfacial peak shear stress shows a significant linear positive correlation with normal stress. The peak shear stress at 150 kPa normal stress is 77.8% higher than that at 50 kPa, which is, basically, consistent with the test results. The effect of moisture content level on peak shear stress presents a trend of increasing first and then decreasing. The interfacial shear strength reaches the maximum at the optimal moisture content level of 13%. When the moisture content level increases to 16%, the effective cohesion of the soil decreases, and the lubrication effect of pore water reduces the interfacial friction coefficient. Consequently, the peak shear stress is reduced by 28.6% compared with the optimal moisture content group, which is in good agreement with the laboratory test trend. When the shear displacement amplitude increases from 1 mm to 3 mm, the interfacial peak shear stress rises rapidly. When the amplitude increases to 5 mm, the growth of shear stress tends to be gentle. The mechanical interlocking effect at the geogrid–soil interface is fully mobilized at a displacement amplitude of 3 mm.

### *4.3. Analysis of Plastic-Strain Evolution of Soil and Interface-Volume-Change Characteristics*

The equivalent plastic-strain-distribution nephograms and vertical-displacement data for silty clay specimens during cyclic shear were extracted to analyze the development characteristics of shear bands and the evolution law of plastic deformation in the soil, and to reveal the mesoscopic causes of interface dilatancy and contraction observed in the

laboratory tests. Under cyclic shear loading, the plastic deformation of silty clay shows an obvious localization characteristic, with a distinct shear band formed above the geogrid–soil interface. Plastic strain is mainly concentrated within the soil range of 0–20 mm above the interface, where the peak equivalent plastic strain reaches 2.8%, representing the core zone of shear deformation. The plastic strain of soil in the depth range of 20–50 mm attenuates rapidly with increasing depth, and the plastic strain in the soil region beyond 50 mm approaches zero. This result identifies the effective influence depth of the shear interaction at the geogrid–silty clay interface, which is in good agreement with the law observed in the laboratory tests that the volume change is mainly controlled by the deformation of soil near the interface.

**Table 8.** Comparison of simulated and experimental results of interfacial peak shear stress under different working conditions.

| Case No. | Combination of Test Variables | Test Value (kPa) | Simulated Value (kPa) | Relative Error |
|---|---|---|---|---|
| 1 | G1-10%-1 mm-50 kPa | 32.6 | 33.8 | 3.70% |
| 2 | G1-13%-1 mm-100 kPa | 58.2 | 56.5 | 2.90% |
| 3 | G1-16%-1 mm-150 kPa | 65.4 | 67.2 | 2.80% |
| 4 | G2-10%-3 mm-50 kPa | 41.5 | 40.3 | 2.90% |
| 5 | G2-13%-3 mm-100 kPa | 72.8 | 71.2 | 2.20% |
| 6 | G2-16%-3 mm-150 kPa | 86.3 | 88.7 | 2.80% |
| 7 | G3-10%-5 mm-50 kPa | 56.2 | 54.8 | 2.50% |
| 8 | G3-13%-5 mm-100 kPa | 97.5 | 99.6 | 2.20% |
| 9 | G3-16%-5 mm-150 kPa | 112.4 | 109.1 | 2.90% |

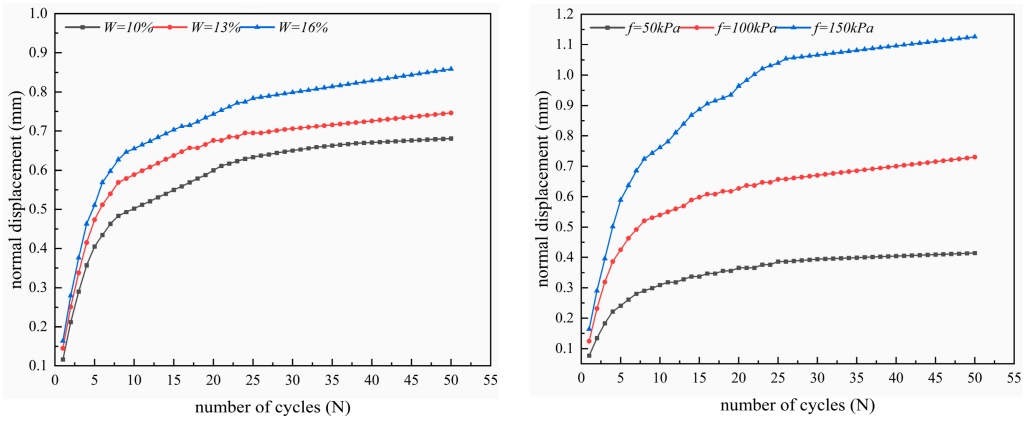
From the perspective of cyclic evolution, during the 1st to 10th cycles, the plastic strain of the soil accumulates rapidly, and the shear band gradually expands from the geogrid–soil interface into the soil interior, corresponding to the stage of rapid increase in normal displacement in the laboratory tests. After 25 cycles, the spatial extent of the shear band and the peak plastic strain remain, basically, stable, and the sliding and rearrangement of soil particles reach a dynamic equilibrium state, corresponding to the macroscopic phenomenon that the volume change effect tends to be stable in the laboratory tests. The distribution and evolution characteristics of soil plastic strain differ significantly under different test conditions. The geogrid under a high moisture content level corresponds to a thicker shear band and a wider distribution range of plastic strain, with the peak plastic strain increased by 52% compared with that at w = 10%. Under the condition of 16% high moisture content, the plastic fluidity of the soil is significantly enhanced. The plastic strain in the shear band is dominated by horizontal shear slip, and the vertical plastic strain component is negative, corresponding to the slight volume contraction at the interface under the high-moisture-content level that was observed in the tests. Under high normal stress conditions, the plastic deformation of the soil is significantly restrained, the thickness of the shear band is obviously reduced, and the peak plastic strain is greatly decreased. This explains the strong inhibitory effect of normal stress on the interface dilatancy, which is in good agreement with the laboratory test result that the maximum normal displacement is only 0.9 mm under 150 kPa normal stress.

The maximum normal displacements of the interface under different working conditions were calculated through numerical simulation and quantitatively compared with the measured results from the laboratory tests, as shown in Table 9. The relative errors between the simulated and experimental values are all controlled within 5%. As the moisture content level increases from 10% to 16%, the interface changes from significant dilatancy to slight dilatancy and, finally, to volume contraction. Meanwhile, under working conditions with more significant dilatancy effects, the mechanical interlocking between soil particles in the

interface shear band and the geogrid is more sufficient, resulting in higher interfacial peak shear stress. The two show an obvious positive correlation, which verifies the conclusion proposed by the laboratory tests that the volume change characteristics can be used as an evaluation index for the mobilization degree of interfacial friction and interlocking. The simulated evolution curves of normal displacement at interfaces under different water contents and normal stresses are shown in Figure 12.

**Table 9.** Comparison of simulated and experimental results of maximum interfacial normal displacement under different working conditions.

| NO. | Combination of Test Variables | Measured Maximum Normal Displacement (mm) | Simulated Maximum Normal Displacement (mm) | Relative Error | Volume Change Characteristics |
|---|---|---|---|---|---|
| 1 | G2-10%-3 mm-100 kPa | 2.2 | 2.11 | 4.10% | dilatancy |
| 2 | G2-13%-3 mm-100 kPa | 1.5 | 1.44 | 4.00% | slight dilatancy |
| 3 | G2-16%-3 mm-100 kPa | −0.4 | −0.38 | 5.00% | volume contraction |
| 4 | G2-13%-3 mm-50 kPa | 2.1 | 2.03 | 3.30% | dilatancy |
| 5 | G2-13%-3 mm-100 kPa | 1.5 | 1.44 | 4.00% | slight dilatancy |
| 6 | G2-13%-3 mm-150 kPa | 0.9 | 0.87 | 3.30% | slight dilatancy |




(**a**) water content (**b**) normal stress

**Figure 12.** Simulation curve of cycle number–normal displacement under different water content level and normal stress.

### *4.4. Analysis of Interface Stiffness-Degradation and Dynamic Characteristics Under Cyclic Loading*

As shown in the shear stress–shear displacement hysteresis curves, the interfacial shear stiffness after different numbers of cycles was calculated, and its cyclic evolution law was analyzed and verified by comparison with the laboratory test results, so as to reveal the internal mechanical mechanism of interface stiffness degradation. The numerical results show that the interfacial shear stiffness exhibits a three-stage evolution characteristic with the increase in the number of cycles: rapid attenuation in the early stage, slow attenuation in the middle stage, and stabilization in the later stage. The stiffness degradation within the 1st to 10th cycles accounts for 76% of the total degradation. After 25 cycles, the stiffness variation is less than 1%, and no significant degradation occurs, basically. This law is in good agreement with the laboratory test results. A comparison between the simulated and experimental shear stiffness values of the reference group after different numbers of cycles is shown in Table 10, and the relative errors between them are all less than 3%.

**Table 10.** Comparison of simulated and experimental shear stiffness of the reference group after different numbers of cycles (Unit: kPa/mm).

| Number of Cycles | 1 Cycles | 5 Cycles | 10 Cycles | 25 Cycles | 50 Cycles |
|---|---|---|---|---|---|
| experimental value | 29.85 | 26.52 | 24.86 | 24.18 | 24.02 |
| simulated value | 28.82 | 25.87 | 24.21 | 23.65 | 22.78 |
| relative error | 3.45% | 2.40% | 2.60% | 2.20% | 5.16% |

From a meso-mechanical perspective, at the initial stage of cyclic shear, the plastic strain of the soil accumulates rapidly, the initial bonding force between particles is continuously destroyed, and the deformation resistance of the interface decreases quickly, which is the main reason for the significant stiffness degradation. With the increase in cycle numbers, the plastic deformation of the soil tends to be stable, and the interface shear resistance gradually changes from being dominated by the initial bonding force to being dominated by friction and mechanical interlocking. Since friction and interlocking exhibit good reversibility and stability during cyclic shear, the interface shear stiffness remains, basically, constant after 25 cycles. The influence laws of different test variables on interface shear stiffness are completely consistent between the numerical simulation and laboratory tests. The greater the geogrid roughness and normal stress, the higher the interface shear stiffness and the slower the degradation rate during cycling. The interface shear stiffness at the optimum moisture content level of 13% is significantly higher than those at 10% (low moisture content) and 16% (high moisture content). The smaller the shear displacement amplitude, the more the interface deformation is dominated by elastic deformation, resulting in a higher shear stiffness (Figure 13).

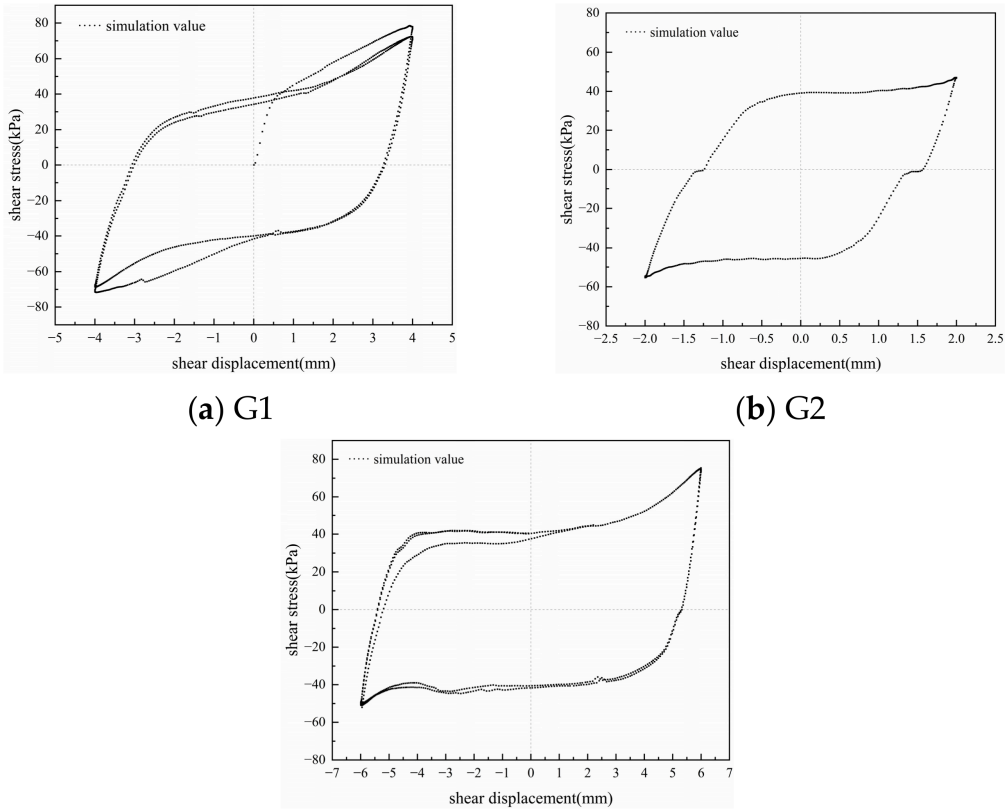



**Figure 13.** Simulated hysteretic curves under different roughness conditions.

## 5. Conclusions

In this study, a combination of laboratory cyclic direct shear tests and numerical simulations was adopted to systematically investigate the macro–meso shear characteristics of the geogrid–silty clay interface under cyclic loading. The regulation laws of four key variables, namely geogrid roughness, soil moisture content, shear displacement amplitude, and normal stress, on the interface shear behavior were analyzed. The intrinsic correlation between the macroscopic mechanical response and mesostructural evolution of the interface was established, and the mechanisms of interface strength degradation, deformation evolution, and energy dissipation during cyclic shearing were clarified. The main conclusions are as follows:

This study investigates the macro–meso shear behavior of the geogrid–silty clay interface under cyclic loading via laboratory cyclic direct shear tests and mesoscopic numerical simulations. The core findings are summarized as follows:

The interface shear strength and shear stiffness show a three-stage cyclic evolution: rapid degradation within the first 1–10 cycles, slow variation in the middle stage, and stabilization after approximately 25 cycles. Higher geogrid roughness and normal stress significantly enhance interface shear strength and suppress cyclic degradation, while the shear strength peaks at the optimum moisture content level of 13%.

The interface-volume deformation is dominated by dilatancy, which is positively correlated with shear strength. Dilatancy is strengthened by increased geogrid roughness and shear displacement amplitude, but strongly inhibited by higher normal stress. The moisture content level governs the volume change mode, which shifts from notable dilatancy to slight contraction as the moisture content level rises from 10% to 16%.

The shear stiffness and damping ratio exhibit opposite cyclic trends, with major changes occurring in the initial 10 cycles. Interface energy dissipation rises rapidly at first and then stabilizes, and is most sensitive to shear displacement amplitude.

The mesoscopic model based on the Modified Cam-Clay criterion accurately reproduces the macroscopic interface response, with relative errors below 5%. Shear stress concentrates at the intersections of geogrid ribs, and the soil zone 0–20 mm above the interface is the primary shear deformation region, which controls the macroscopic cyclic degradation and volume change of the interface.

**Author Contributions:** L.W.: conceptualization, methodology, investigation, and writing—original draft; Z.Z.: data curation, formal analysis, and validation; Z.S.: resources, visualization, and software support; J.W. (corresponding author): supervision, project administration, and writing—review and editing, funding acquisition, and correspondence; and H.L.: investigation, methodology, and formal analysis. All authors have read and agreed to the published version of the manuscript.

**Funding:** Taishan Scholars Program No. tstp20231240, Science and Technology Program of Department of Transportation of Hebei Province, 2025 (No. CZ202505).

**Institutional Review Board Statement:** Not applicable.

**Informed Consent Statement:** Not applicable.

**Data Availability Statement:** Data available on request from the authors. The data that support the findings of this study are available from the corresponding author, JinCheng Wei, upon reasonable request.

**Conflicts of Interest:** Authors Liang Wang, Zhice Zhao, and Hongxing Li were employed by the company Cangzhou Transportation Development (Group) Co., Ltd. The remaining authors declare that the research was conducted in the absence of any commercial or financial relationships that could be construed as a potential conflict of interest.

## References


1. Jia, Y.; Guo, Y.; Morsy, A.M.; Zornberg, J.G.; Zhang, J.; Xie, M.; Zheng, Y. Experimental evaluation on bearing performance of tire cell-geogrid reinforced subgrades. *Transp. Geotech.* **2026**, *59*, 101944. [CrossRef]
2. Irani, R.; Saba, H.R.; Ardakani, A.R.M.; Shahverdi, M.R.; Madadi, A.; Memari, N. Laboratory Experimental Study of Soil Improvement in Saveh City Using Micro-Silica and Geogrid Via Dynamic Simple Shear Testing. *Indian Geotech. J.* **2026**, 1–21, *prepublish*. [CrossRef]
3. Lu, J.; Wang, J.-Q.; Su, Z.-J.; Jia, M.-C.; Zou, C.-H. Influence of Gravel Size and Geogrid Aperture on Performance of Geosynthetic-Encased Stone Column: DEM-FDM Coupled Numerical Investigation. *Appl. Sci.* **2026**, *16*, 1610. [CrossRef]
4. Jing, T.L.; Chen, B.G.; Fei, Y.L. Effect of Particle Size on Shear Behavior of Geogrid–Aggregate Interface under Cyclic Normal Loading. *J. Mater. Civ. Eng.* **2025**, *37*, 04025431. [CrossRef]
5. Liu, F.-Y.; Li, J.-T.; Ying, M.; Ge, M.; Fu, J. Effect of Particle Shape on Cyclic Shear Behavior of Granular Mixtures–Geogrid Interface. *Transp. Res. Rec.* **2025**, *2679*, 371–383. [CrossRef]
6. Chen, Q.; Wei, H.; Li, X.; Zou, B.; Deng, Y.; Kong, B. Experimental visualization of soil arching evolution and collapse in pile-supported embankments under cyclic loading. *Ain Shams Eng. J.* **2026**, *17*, 104059. [CrossRef]
7. Liu, Y.; Zhang, H.; He, T.; Zhou, X.; Qin, Z. Reloading experimental research on the mechanical characteristics and failure mechanism of sandstone samples considering pre-peak cyclic loading. *Bull. Eng. Geol. Environ.* **2026**, *85*, 178, Correction in *Bull. Eng. Geol. Environ.* **2026**, *85*, 245. https://doi.org/10.1007/s10064-026-04942-y.. [CrossRef]
8. Liu, Z.; Ma, X.; Zhou, D.; Lu, L.; Zhang, H.; Bai, Y.; Han, H. The geological origins and soil properties of loess-like silty clay: A case study in the jinan area. *Sci. Rep.* **2024**, *14*, 12612. [CrossRef]
9. Jiang, X.; Hou, W.; Zhang, D.; Guo, Z.; Wang, D.; Wang, X. Experimental Study on Crack Evolution Characteristics in Guar Gum-Modified Silty Clay. *Polymers* **2025**, *17*, 1841. [CrossRef]
10. Chen, G.; Yang, W.; Pan, Y.; Zheng, Y.; Zhang, H.; Shao, S.; Lu, F.; Yang, C.; Guo, L. Study on accumulation deformation characteristics of silty clay based on dynamic triaxial tests. *Sci. Rep.* **2025**, *15*, 11448. [CrossRef]
11. Ma, X.; Bai, F. The role of geogrid aperture shape and size in strengthening aeolian sands: Insights from a coupled DEM-FDM approach. *Comput. Geotech.* **2025**, *180*, 107067. [CrossRef]
12. Xu, L.; Wang, R.; Liu, Q.; Chen, J.; Wang, X.; Meng, Q. Effect of particle size distribution on monotonic direct shear characteristics of geotextile/geogrid-calcareous sand interface. *Appl. Ocean Res.* **2023**, *137*, 103601. [CrossRef]
13. He, R.; Lu, J.; Gao, J.; Li, Y.; Li, H.; Deng, F. Variation Characteristics and Influential Factors of Unfrozen Water Content across Different Types of Soils. *J. Cold Reg. Eng.* **2026**, *40*, 04026007. [CrossRef]
14. Xian, J.; Pei, W.; Lai, Y.; Zhang, M.; Yu, F.; Chen, Y. Uniaxial compressive behavior of frozen silty clay at extreme low temperature with varying initial water content. *Cold Reg. Sci. Technol.* **2026**, *244*, 104825. [CrossRef]
15. Sun, Y.; Guan, Y.; Huang, X. Mechanical behavior of sand reinforced with conventional and NPR geogrids: A numerical study on structural influence. *Structures* **2025**, *81*, 110170. [CrossRef]
16. Soehardi, F.; Hakam, A.; Thamrin, R.; Mera, M. Optimization of Bearing Capacity of Sandy Soil Using Geosynthetic: An Experimental Study on Sand Types and Reinforcement Material Variations. *Ann. Chim.-Sci. Matériaux* **2025**, *49*, 203–212. [CrossRef]
17. Bandyopadhyay, S.; Parulekar, Y.M.; Ramakrishna, P.; Pandey, J.K.; Chattopadhyay, J. Evaluation of Soil Dynamic Properties Using Shake Table Tests on Laminar Shear Box and Its Numerical Verification. *Int. J. Geomech.* **2026**, *26*, 04026016. [CrossRef]
18. Huang, H.M.; Cui, D.Z.; Zhang, J.L. Effect of initial static sheet stress on cyclic properties of soft claim in constant volume simple sheet tests. *Oil Dyn. Earthq. Eng.* **2025**, *197*, 109547. [CrossRef]
19. Li, J.; Gao, C.; Liu, F. Cyclic Shear Tests and DEM Analysis of Soil-Rock Mixture-Concrete Interfaces with Different Fine Contents. *Int. J. Civ. Eng.* **2026**, *24*, 569–584. [CrossRef]
20. Chun, J.C.; Saito, A.; Hino, T. Effect of Surface Roughness on Soil-Geogrid/Geotextile Interface Shear Strengths. *Int. J. Geosynth. Ground Eng.* **2024**, *10*, 43. [CrossRef]
21. Shoukat, T.; Yoo, P.J.; Kim, J.H.; Kim, Y. Comparative study on fiber reinforcement and geogrid for enhancing the long-term performance of asphalt pavements against rutting failure. *Constr. Build. Mater.* **2025**, *499*, 144083. [CrossRef]


**Disclaimer/Publisher's Note:** The statements, opinions and data contained in all publications are solely those of the individual author(s) and contributor(s) and not of MDPI and/or the editor(s). MDPI and/or the editor(s) disclaim responsibility for any injury to people or property resulting from any ideas, methods, instructions or products referred to in the content.